Unconventional fabrication of 2D nanostructures and graphene edges

Bellunato, A.

CHAPTER 5

One-pot inert mask lithography of edge narrowed graphene nanoribbons directly contacted to metallic electrodes

Graphene nanoribbons, namely nanometric stripes of graphene constrained into a single dimension, are formed via inert mask lithography underneath metallic nanorods. The masks are prepared via the microtomy of metallic thin films embedded within polymeric scaffolds and precisely deposited on top of a graphene monolayer. The inertness of the metallic masks – here gold and aluminium –allows the precise narrowing of graphene into nanoribbons under different etching environments, thus also permitting the control over the edge chemistry of graphene, while protecting the basal plane. Remarkably, the nanoribbons can be electrically measured by converting the metallic mask into in-situ electrodes by local melting of the metal using a laser pulse. Our method proposes a simple, direct approach towards the design of chemically tailored, scalable, and electrically connected graphene nanoribbons.

Publication in preparation: Amedeo Bellunato, Alex van der Ham and Grégory F. Schneider.

5.1 Introduction

Remarkable step-forwards in graphene synthesis and clean transfer protocols prompted the expectations for future applications of graphene in numerous technological fields[1] such as energy storage[2], filtration[3], diagnostic[4] and even consumable electronics[5,6]. Thus, the growing demand of graphene also requires precisely patterned graphene films, particularly into miniaturized architectures such as quantum dots and nanoribbons[7–10]. For instance, precisely designed graphene nanoribbons, namely nanometric thin strips of graphene,[11] can widen the band-gap of graphene from 0 eV up to 10 eV, yielding graphene based transistors for logic operations[12,13], operating as gas sensors[14], thermosensors[15] or photodetectors[16].

In this chapter, graphene nanoribbons are fabricated using the shadowing of a metallic mask. Metallic masks are prepared by sectioning metallic thin films embedded in a polymer scaffold using microtomy[17], and converted into metallic nanorods. Next, the nanorods are aligned over the surface of graphene and are exposed to reactive ion etching. Upon etching, the nanorod covers the graphene underneath, yielding a graphene nanoribbon. The nanorod forms an inert interface with graphene, preserving the integrity and the chemical structure of the basal plane of graphene, as opposed to polymeric masks employed in conventional lithography of graphene[18]. In fact, polymeric masks generate residuals that uncontrollably contaminate the graphene, with detrimental consequences for the chemistry of graphene, both at the basal plane and at the edges[19,20].

The use of metallic masks allows the sculpting of graphene ribbons also in harsh and highly reactive environments, permitting the selective functionalization of graphene, otherwise not compatible with standard lithographic approaches. Metallic masks physically hinder the basal plane of the graphene underneath, forcing the etching to proceed via the edges. As a result, metallic masks permit the fabrication of graphene nanoribbons selectively functionalized at the edges in highly reactive environments such as reactive ion etching, organic solvents and under UV irradiation, thanks to the physical protection of a nanorod prepared via microtomy.

Importantly, microtomy allows the versatile fabrication of graphene nanoribbons, controllably yielding nanorods varying between few nanometres up to hundreds

of nanometres in width and extending over hundreds of micrometres in length. Additionally, we demonstrate the possibility of locally melting the mask by laser pulse irradiation, yielding in-situ controlled electrodes for the electrical characterization of the graphene nanoribbons, therefore achieving the single step fabrication of graphene nanoribbons and their electrodes.

5.2 Results and discussion

Metallic masks are prepared in the form of nanorods sectioned via microtomy starting from metallic thin films and deposited over supported graphene monolayers (Figure 5.1). Microtomy of metallic nanorods was first introduced by Whitesides and co-workers[17], who showcased that the slicing of metallic thin films using an ultra-sharp diamond knife[21] can be used as an unconventional approach to fabricate plasmonic resonators[22]. In Figure 5.1, a metallic film embedded within a polymer scaffold (Figure 5.1 a-i to a-iii) is sectioned with nanometric precision using a diamond knife (Figure 5.1 b-i). The cut yields polymeric slabs embedding metallic nanorods extending over several micrometres in length. The polymer/nanorod/polymer slab slides from the blade to float over a water reservoir at the back of the diamond knife. A perfect loop ring exploits the surface tension of the water to withdraw the slab from the reservoir. Subsequently, the ring is placed over a graphene substrate (Figure 5.1b-ii), while the water evaporates landing the slab on the graphene. In the meantime, a microneedle attached to a step-manipulator pins the slab during the water evaporation, allowing the proper alignment of the metallic mask over the surface of the graphene. This step, notably, permits the deposition of nanorods over pre-patterned electrodes for the electrical characterization of the nanoribbon.

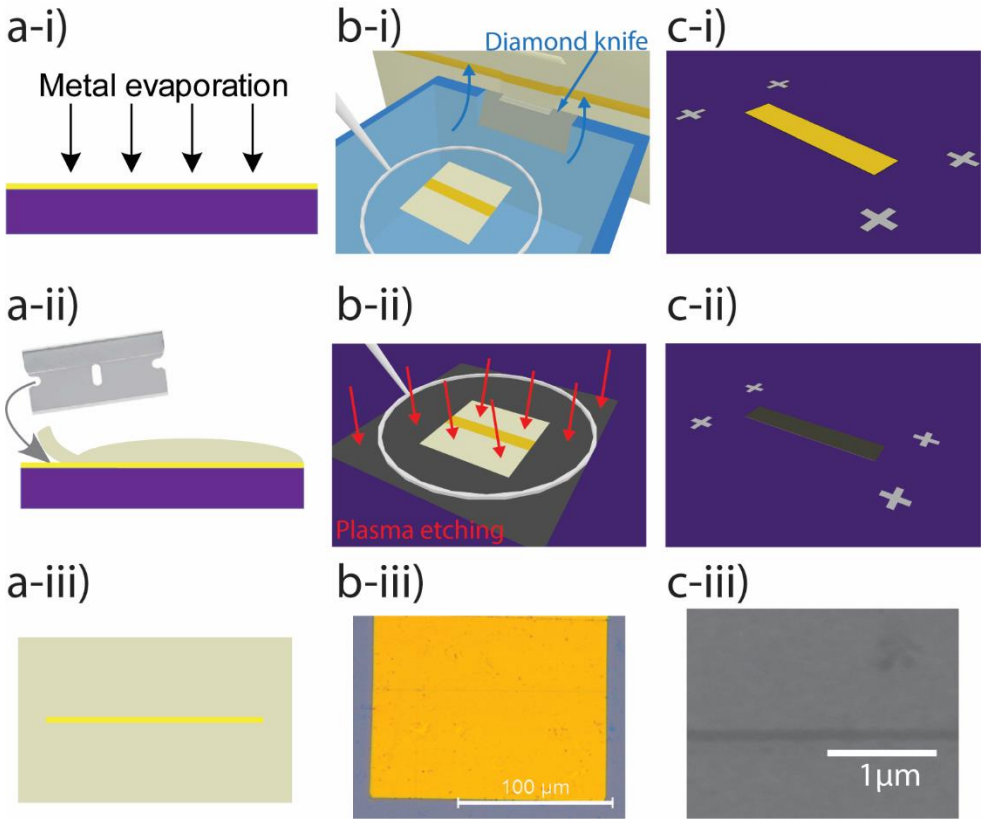

Figure 5.1. Fabrication of a graphene nanoribbon underneath a metallic nanorod prepared via microtomy. a-i) to a-iii) Embedding of the metallic thin film into the polymer scaffold. The metallic film is evaporated over a Si/SiO_2 wafer. A drop of polymer is casted and cured on the surface of the metal while a razor blade lifts the gold and the polymer from the substrate. At last, the gold is fully embedded in the polymer. b-i) Microtomy of metallic thin films into metallic inert masks. The polymer is sectioned by a diamond knife forming polymeric slabs supporting metallic nanorods. b-ii) Transfer of the polymer slab over the graphene film using a perfect loop. Plasma etching removes the polymer slab and the graphene surrounding the metallic mask. b-iii) Optical micrograph of a slab over the graphene film. c-i) and c-ii) The metallic mask is removed from the substrate via sonication or wet etching, uncovering the mask. c-iii) Scanning electron micrograph, SEM, of a graphene nanoribbon fabricated via inert mask lithography.

Reactive ion etching removes the polymer slab and the graphene surrounding the mask until the boundaries of the nanorod, Figure 5.1 c-i to c-iii. The mask covers and protects the basal plane of graphene, forcing the etching to proceed via the edges of graphene, thus promoting the control over the chemical composition of the edges while preserving the integrity of the basal plane. Lastly, the metallic inert

mask is either removed via sonication, or melted in the centre forming (in situ) electrodes for the characterization of the nanoribbons.

Accordingly, the edge narrowing via reactive ion etching yields nanoribbons narrower than the width of the covering mask, as shown by the scanning electron microscopy, SEM, micrograph of an 80 nm graphene nanoribbon (Figure 5.2a) formed in H_2 plasma (0.3mbar and 60W) underneath 300 nm wide aluminium mask (inset Figure 5.2a). Thus, while the metallic nanorod protects the surface of graphene, limited diffusion of reactive species proceeds underneath the mask through etching of the edges. As a result, the mask protects the basal plane of graphene yielding thin nanoribbons uniformly extending over several micrometres in length. The AFM topography image in Figure 5.2b shows the 80nm wide graphene nanoribbon (Figure 5.2c) uniformly extending over one micrometre in length without breakings. The nanoribbon presents some poly (methyl methacrylate), PMMA, residuals, result of the PMMA assisted deposition of the graphene monolayer on the Si/SiO_2 support. Finally, the Raman mapping of the nanoribbon shown in Figure 5.2d extends uniformly over a window of three micrometres, showing a Raman signature (inset) characteristic of a high quality, single layer graphene, as suggested also by a 2D band (at 2684 cm^{-1}) over G band (at 1590 cm^{-1}) ratio above one[23,24]. The ratio between the D peak (at 1341 cm^{-1}) and the G band is lower than one, indicating a high quality graphene[25], confirming the protective role of the metallic mask, and in agreement with both the scanning electron microscopy, SEM, and the atomic force microscopy, AFM, images.

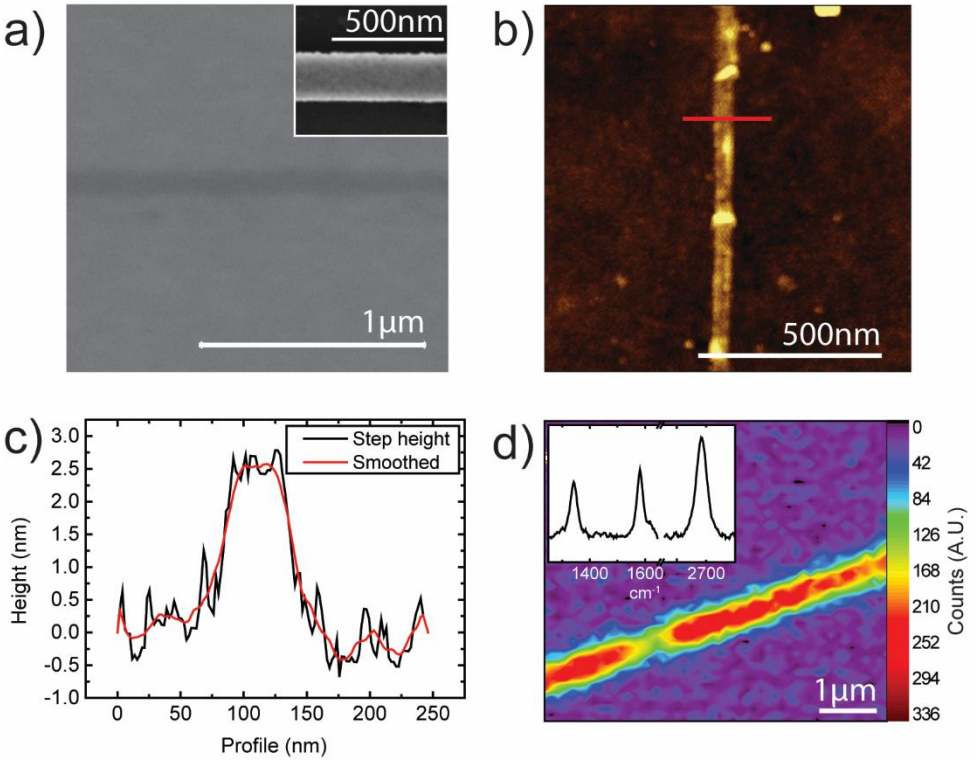

Figure 5.2. Characterization of a graphene nanoribbon formed from a 300nm wide aluminium mask. a) Scanning electron microscope, SEM, micrograph of a graphene nanoribbon on SiO_2 extending over 1 µm. Inset: SEM micrograph of the 300 nm aluminium nanorod prepared by microtomy and used as etching mask. b) and c) AFM intermittent contact mode image and step-height (red line in b)) of an 80 nm wide graphene nanoribbon. d) Raman mapping of the 2D band of the graphene nanoribbon at 2684 cm^{-1}. Inset: Raman signature of the nanoribbon.

At first, the metallic mask is supported by a polymer slab, which allows the precise transfer and alignment of the nanorod from the microtome knife to the surface of the graphene. A microneedle connected to a microstep manipulator pins the slab, securing its position over the surface of graphene during the transfer. Figure 5.3a shows the optical micrograph of a graphene film deposited over two gold pads 50 nm thick at about 20 µm distance. The 300 nm wide and 150 nm thick aluminium nanorod is deposited precisely across the two electrodes, electrically connecting them with a total resistance of about R_{Al} = 700 Ω, yielding a resistivity $\rho_{Al} = 6x10^{-6}$ Ωm. This value matches the resistivity of aluminium, around $2x10^{-8}$ Ωm, taken in

consideration the high contact resistance at the interface between the gold, the graphene and the aluminium.

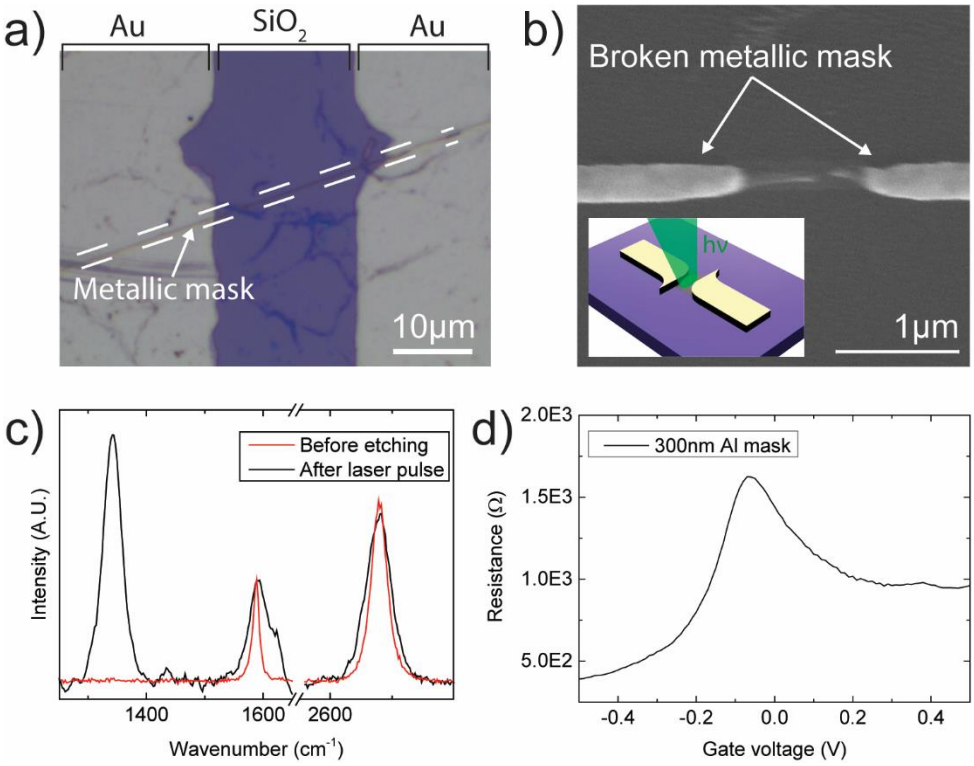

Figure 5.3. Laser induced formation of metallic electrodes. a) Optical micrograph of a graphene nanoribbon covered by a 300 nm wide aluminium nanorod connecting two gold contact pads. b) Rupture of the nanorod due to thermal shock after exposure to a 532 nm laser beam at 58mW for 2 s. Inset: schematization of the rupture process induced by the laser. c) Raman spectra of the graphene before fabricating the nanoribbon and after the opening of the electrodes by a 5s laser irradiation. d) IV characteristic of the 80 nm wide nanoribbon patterned under a 300 nm wide aluminium mask.

Subsequently, reactive ion etching removes the polymer and sculpts a graphene nanoribbon underneath the metallic mask. The nanorod remains over the surface of graphene protecting the basal plane from etching and physically contacting the nanoribbon. Thus, the local rupture of the metallic mask yields a set of independent metallic electrodes already aligned over the graphene nanoribbon, Figure 5.3b. This step, importantly, avoids the demand for further lithographic processing otherwise required to design electrodes for the electrical

characterization of the graphene nanoribbons. Particularly, the lithography of the electrodes would involve polymeric masks, leading to contaminations, beyond the intrinsic difficulties of designing nanometric aligned electrodes (see Figure 5.1 of Appendix III). Thus, in order to form the electrodes, the nanorod is broken locally by shining a 532 nm, 58 mW laser through a 100X objective and using a mechanical shutter to limit the exposure time. The irradiation energy of the laser beam is converted into thermal energy absorbed by the metallic nanorod[26]. The high density of power causes an abrupt expansion of the metallic nanorod, a thermal shock, causing the rupture. The mechanical shutter avoids prolonged exposure times. In fact, the prolonged irradiation of such a high intensity laser might compromise the graphene nanoribbon. An exposure time of 2 s over a 300nm wide aluminium nanorod yields a rupture in the nanorod tens of nanometres long, forming independent electrodes. Notably, for the Raman investigation the laser was shone for 5s over the nanorod, in order to open a gap wide enough to allow the characterization of the graphene nanoribbon by Raman spectroscopy, Figure 5.3c. In this case, the I(D)/I(G) ratio is above one, highlighting the presence of damages induced by the rupture of the nanorod, probably due to the prolonged exposure of the graphene to the laser beam. Nonetheless, the Raman signature indicates the presence of the graphene nanostructure yielding a conductive nanoribbon. For 2s exposure (thus limited exposure), the resistivity of the graphene is around R = 1.5 KΩ for a square resistance $R_{sq.}$[27] above 1 KΩ, considering an average electrode spacing in the order of few hundreds of nanometres over an 80 nm wide ribbon, Figure 5.3d. The electrical characteristic is measured against a gating potential applied from a 1 M solution of KCl in ultra pure water and against an Ag/AgCl electrode. The plot shows the rise in resistivity typical of the cone band structure of graphene, shifting from around 500 Ω up to about 1.75 kΩ and reaching its apex at the Dirac point[28], at slightly negative gating potential.

Metallic masks offer inert interfaces for the sculpting of graphene, drastically limiting the source of contaminations at least compared to conventional lithography[29]. Furthermore, the physical mask protects the surface of graphene forcing the sculpting of the nanoribbons via the edges, also regulating the chemistry at the edges. Thus, the geometry of the mask and the etching environment actively modify the physical and chemical properties of graphene. For instance, the reduction of the mask width directly reflects a narrowing of the graphene nanoribbon sculpted underneath. Raman spectroscopy in Figure 5.4a

shows an increase of I(D)/I(G) ratio with decreasing ribbons width. In fact, the edges activate a defect related Raman mode referred to as D at 1340 cm^{-1}. Its intensity is measured with respect to the G band at 1590 cm^{-1} and increases with the amount of edges[30], thus inversely proportional to the width of the nanoribbons (see Figure 5.2 of Appendix III), Figure 5.4b.

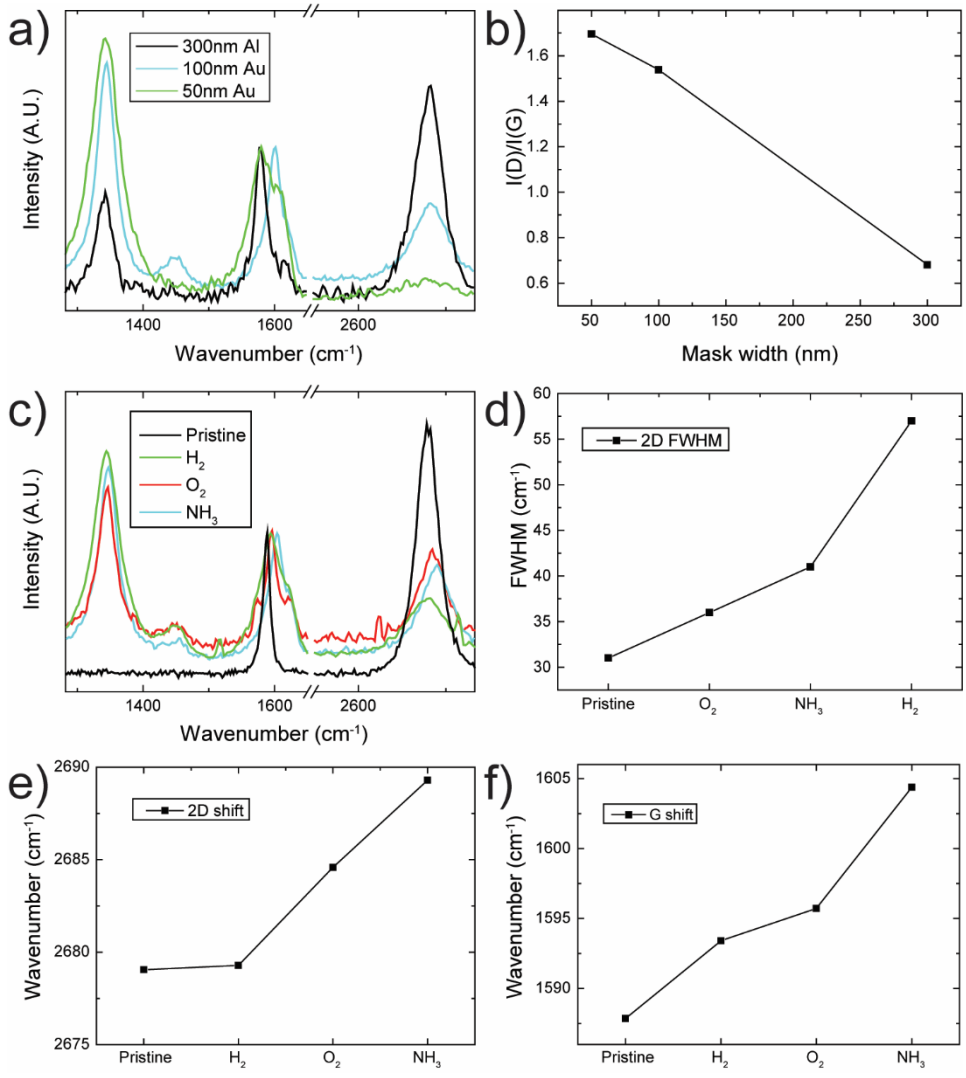

Figure 5.4. Raman characterization of graphene nanoribbons produced under metallic masks. a) Raman spectra of graphene nanoribbons patterned underneath metallic masks respectively of 50nm gold, 100 nm gold and 300 nm Al. b) I(D)/I(G) ratio for the different mask sizes. c) Raman spectra of graphene nanoribbons formed under 100 nm wide metallic

masks in H_2, O_2 and NH_3 plasma. d) G-peaks position of the nanoribbons illustrated in panel c). e) and f) 2D peak position shift and full width half maximum, FWHM, for graphene nanoribbons etched respectively in H_2, O_2 and NH_3 plasma.

Similarly, varying the etching environment impacts on the chemistry of the edges of graphene, thus on its properties such as the electronic structure. Accordingly, Raman spectroscopy highlights differences in the graphene structures for nanoribbons designed under 100 nm wide nanorods respectively in H_2, O_2 and NH_3 plasma, all at 0.3 mbar 60 W, Figure 5.4c. The I(D)/I(G) intensity is constant among the three different structures, as expected for masks of the same size. Nonetheless, the different etching gases affect differently the chemistry of the edges. The results can be monitored in terms of shifts in the 2D and G Raman peaks of the graphene nanoribbons[32–39] and in the full-width half maximum, FWHM, intensity of the 2D peaks. Accordingly, at fixed D band position, the G and 2D bands shift differently for different etching environments, Figure 5.4c, along with a widening of the 2D peaks, as confirmed in Figures 5.4d. Such variations in terms of 2D peaks are in line with the nanostructuring of the graphene sample and the increased amount of edge carbons atoms composing the nanostructure[30,35,40]. G and 2D bands are particularly sensitive to the edge chemistry, and the electrical properties of narrow graphene nanostructures (with high amount of edges) are more influenced by the chemical functionalization of the edge atoms. Heteroatoms linked to the lattice of graphene are characterized by different electro-negativities and electronic energy levels, yielding different charge doping levels via holes and electrons injections. Particularly, electronegative atoms like oxygen and nitrogen are expected to induce p-doping in the structure of graphene, donating holes and withdrawing electrons. This, supposedly, induces a red-shift in the G and 2D band of graphene[31,41]. Accordingly, comparing Figure 5.4e and Figure 5.4f we observe a more prominent red-shift on the G and 2D peaks of nanoribbons etched via O_2 and NH_3, while the red-shift is weaker for elemental hydrogen, the same trend is not observed for the D peak. If we compare the results with respect to the pristine graphene, we can observe a relevant shift for all the three etching gases. This can be the result of a combined effect of the nanostructuring together with elemental doping. We can observe that, especially in the case of NH_3 and O_2, the composition of the gas environment appears to offer a more visible effect on the control of the edge chemistry. In fact, doping varies the amount of electrons and holes density in the band structure of graphene, modifying also the 2D band of graphene during

Raman spectroscopy[24]. The result is a shift in the 2D band wavelength together with a widening of its FWHM. Importantly, observing the Raman spectra in Figure 5.4, we might need to consider the presence of residual oxygen traces during all the etching processes, which remains during the low vacuum pumping, and that can strengthen the doping effect, particularly in the case of hydrogen functionalization.

Additionally, metallic masks are chemically resistant to several reactive environments. For instance, metallic masks composed of gold and aluminium are insoluble in organic solvents (as opposed to polymeric masks used in conventional lithography). Thus, the use of metallic masks opens possibilities to address selectively the edge chemistry of graphene nanoribbons in organic solvents. For instance, graphene nanoribbons were functionalized using ferrocyanol azide under UV irradiation. More precisely, a graphene nanoribbon was first etched under a 300 nm wide mask in H_2 atmosphere and further exposed to ferrocyanol azide in a solution of tetrahydrofuran, THF, under UV irradiation at 365 nm. Ferrocyanol azide releases N_2 under UV irradiation, forming highly reactive radicals proved to be reactive with polyaromatic hydrocarbons, nanographenes and carbon nanotubes[42,43]. During the reaction, the mask protects the surface of graphene, while the ferrocyanol radicals react with the hydrogenated edges of graphene, as proposed in Figure 5.5a. The Raman spectra of the graphene nanoribbon is proposed Figure 5.5b, green line: the reaction with ferrocyanol azide in THF under UV for half an hour, Figure 5.5b blue line, causes a strong increase of the D band of graphene. The D band increase is ascribed to the functionalization of graphene with the iron ligand, in agreement with what is observed for the edge functionalization of graphene with nitro-aryl radicals[29]. Most importantly, we can observe a strong red-shift in the positions of the G and 2D bands, in line with the red shift expected for nitrogenated linkers.

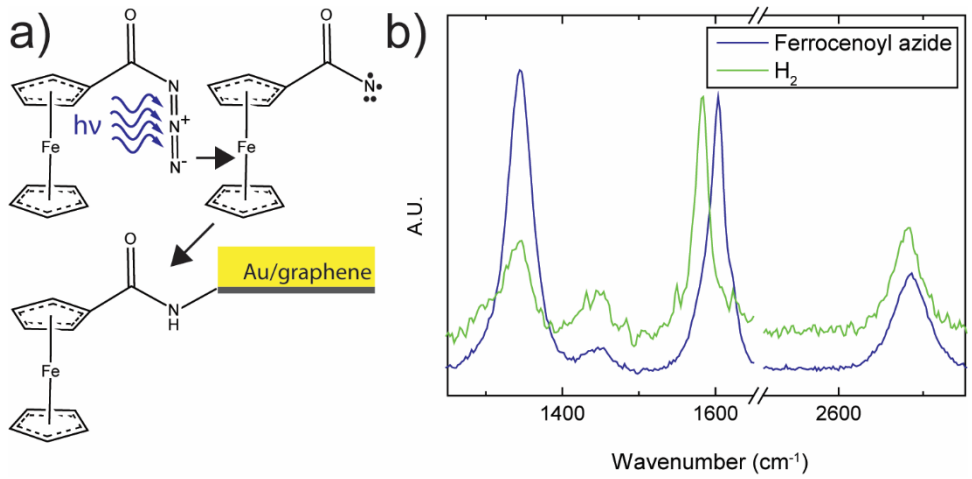

Figure 5.5. Edge functionalization of a graphene nanoribbon using ferrocyanol azide. a) Schematics of the edge functionalization of a graphene nanoribbon formed under a gold mask by exposure to ferrocyanol azide activated by UV irradiation. b) Comparison of the Raman spectra of nanoribbons prepared by H_2 plasma etching under 300 nm wide mask (green) and after reaction with ferrocyanol azide (blue).

Importantly, the metallic mask allows the functionalization of the edges of graphene via the reaction with ferrocyanol azide in organic solvents under UV irradiation, otherwise impossible with conventional lithographic masks such as PMMA. In fact, the combined effect of the organic solvent and the UV irradiation would most likely dissolve PMMA, uncovering the surface of graphene yielding a direct reaction of the ferrocyanol azide with the basal plane of graphene.

5.3 Conclusions

To conclude, we developed a lithographic approach for the scalable synthesis of graphene nanoribbons with controlled edge terminations, where graphene nanoribbons are directly electrically connected with metallic electrodes prepared in-situ. The use of metallic masks introduces enormous advantages over polymeric masks: the chemical inertness of the mask allows for the specific edge functionalization of graphene in organic solvents. The inertness of the metallic masks allows also the prolonged exposure of the graphene to harsh etching environments and reactive compounds. Separately, laser pulse induced thermal shock allows to employ the nanorods as in-situ deposited electrodes, preventing the post-processing of the graphene nanoribbons, and permitting the in-situ and

direct measurement of chemically derivatized nanoribbons. These results mark a step forward towards the simple nanofabrication of graphene-based nanoarchitectures with tunable, controllable edge chemistry.

5.4 References

(1) Zurutuza, A.; Marinelli, C. *Nat. Nanotechnol.* **2014**, *9* (10), 730–734.

(2) Liu, J. *Nat. Nanotechnol.* **2014**, *9* (10), 739–741.

(3) Jiang, Y.; Biswas, P.; Fortner, J. D. *Environ. Sci. Water Res. Technol.* **2016**, *2* (6), 915–922.

(4) Kostarelos, K.; Novoselov, K. S. *Nat. Nanotechnol.* **2014**, *9* (10), 744–745.

(5) Ahn, J.-H.; Hong, B. H. *Nat. Nanotechnol.* **2014**, *9* (10), 737–738.

(6) Torrisi, F.; Coleman, J. N. *Nat. Nanotechnol.* **2014**, *9* (10), 738–739.

(7) Sadeghi, H.; Algaragholy, L.; Pope, T.; Bailey, S.; Visontai, D.; Manrique, D.; Ferrer, J.; Garcia-Suarez, V.; Sangtarash, S.; Lambert, C. J. *J. Phys. Chem. B* **2014**, *118* (24), 6908–6914.

(8) Saha, K. K.; Drndić, M.; Nikolić, B. K. *Nano Lett.* **2012**, *12* (1), 50–55.

(9) Puster, M.; Rodrıguez-Manzo, J. A.; Balan, A.; Drndic, M. *ACS Nano* **2013**, *7* (12), 11283–11289.

(10) Ritter, K. a; Lyding, J. W. *Nat. Mater.* **2009**, *8* (3), 235–242.

(11) Celis, A.; Nair, M. N.; Taleb-Ibrahimi, A.; Conrad, E. H.; Berger, C.; de Heer, W. A.; Tejeda, A. *J. Phys. D. Appl. Phys.* **2016**, *49* (14), 143001.

(12) Schwierz, F. *Nat. Nanotechnol.* **2010**, *5* (7), 487-496.

(13) Zhan, B.; Li, C.; Yang, J.; Jenkins, G.; Huang, W.; Dong, X. *Small* **2014**, *10* (20), 1-24.

(14) Yavari, F.; Koratkar, N. *J. Phys. Chem. Lett.* ***2012****, 3 (13), 1746–1753*.

(15) Davaji, B.; Cho, H. D.; Malakoutian, M.; Lee, J. K.; Panin, G.; Kang, T. W.; Lee, C. H. *Sci. Rep.* **2017**, *7* (1), 8811.

(16) Zomer, P.; Guimarães, M. *Appl. Phys. Lett.* **2014**, 105, 013101.

(17) Xu, Q.; Rioux, R. M.; Dickey, M. D.; Whitesides, G. M. *Acc. Chem. Res.* **2008**, *41* (12), 1566–1577.

(18) Fischbein, M. D.; Drndic, M., *Appl. Phys. Lett.* **2018**, 93, 113107.

(19) Gass, M. H.; Bangert, U.; Bleloch, A. L.; Wang, P.; Nair, R. R.; Geim, A. K. *Nat. Nanotechnol.* **2008**, *3* (11), 676–681.

(20) Ishigami, M.; Chen, J. H.; Cullen, W. G.; Fuhrer, M. S.; Williams, E. D. *Nano Lett.* **2007**, *7* (6), 1643–1648.

(21) Arjmandi-Tash, H.; Bellunato, A.; Wen, C.; Olsthoorn, R. C.; Scheicher, R. H.; Zhang, S.-L.; Schneider, G. F. *Adv. Mater.* **2017**, 1703602.

(22) Wiley, B. J.; Lipomi, D. J.; Bao, J.; Capasso, F.; Whitesides, G. M. *Nano Lett.* **2008**, *8* (9), 3023–3028.

(23) Ferrari, A. C.; Basko, D. M. *Nat. Nanotechnol.* **2013**, *8* (4), 235–246.

(24) Ferrari, A. C. *Solid State Commun.* **2007**, *143* (1–2), 47–57.

(25) Ferrari, A. C.; Robertson, J. *Phys. Rev. B* **2000**, *61* (20), 14095–14107.

(26) Zhou, L.; Lu, J.; Yang, H.; Luo, S.; Wang, W.; Lv, J.; Qiu, M.; Li, Q. *Appl. Phys. Lett.* **2017**, *110* (8), 081101.

(27) Peng, S.; Jin, Z.; Ma, P.; Zhang, D.; Shi, J.; Niu, J.; Wang, X.; Wang, S.; Li, M.; Liu, X.; Ye, T.; Zhang, Y.; Chen, Z.; Yu, G. *Carbon* **2015**, *82*, 500–505.

(28) Castro Neto, a. H.; Peres, N. M. R.; Novoselov, K. S.; Geim, A. K. *Rev. Mod. Phys.* **2009**, *81* (1), 109–162.

(29) Choi, W.; Shehzad, M. A.; Park, S.; Seo, Y. *RSC Adv.* **2017**, *7* (12), 6943–6949.

(30) Casiraghi, C.; Hartschuh, A.; Qian, H.; Piscanec, S.; Georgi, C.; Fasoli, A.; Novoselov, K. S.; Basko, D. M.; Ferrari, A. C. *Nano Lett.* **2009**, *9* (4), 1433–1441.

(31) Ferrari, A. C.; Meyer, J. C.; Scardaci, V.; Casiraghi, C.; Lazzeri, M.; Mauri, F.; Piscanec, S.; Jiang, D.; Novoselov, K. S.; Roth, S.; Geim, A. K. *Phys. Rev. Lett.* **2006**, *97* (18), 187401.

(32) Wang, X.; Li, X.; Zhang, L.; Yoon, Y.; Weber, P. K.; Wang, H.; Guo, J.; Dai, H. *Science.* **2009**, *324* (5928).

(33) Rybin, M.; Pereyaslavtsev, A.; Vasilieva, T.; Myasnikov, V.; Sokolov, I.; Pavlova, A.; Obraztsova, E.; Khomich, A.; Ralchenko, V.; Obraztsova, E. *Carbon* **2016**, *96*, 196–202.

(34) Piazza, A.; Giannazzo, F.; Buscarino, G.; Fisichella, G.; La Magna, A.; Roccaforte, F.; Cannas, M.; Gelardi, F. M.; Agnello, S. *Phys. status solidi* **2016**, *213* (9), 2341–2344.

(35) Iqbal, M. W.; Iqbal, M. Z.; Jin, X.; Hwang, C.; Eom, J. *ACS Appl. Mater. Interfaces* **2014**, *6*, 4207.

(36) Xie, W.-G. W.; Lai, X.; Wang, X.-M. X.; Wan, X.; Yan, M.-L.; Mai, W.-J.; Liu, P.-Y.; Chen, J.; Xu, J. *Spectrosc. Lett.* **2014**, *47* (6), 465–470.

(37) Xie, L.; Jiao, L.; Dai, H. *J. Am. Chem. Soc.* **2010**, *132* (42), 14751–14753.

(38) Stampfer, C.; Wirtz, L.; Jungen, A.; Graf, D.; Molitor, F.; Hierold, C.; Ensslin, K. *Appl. Phys. Lett.* **2007**, *91* (24), 241907.

(39) Stampfer, C.; Molitor, F.; Graf, D.; Ensslin, K.; Jungen, A.; Hierold, C.; Wirtz, L. *Appl. Phys. Lett.* **2007**, *91* (24), 241907.

(40) Eckmann, A.; Felten, A.; Mishchenko, A.; Britnell, L.; Krupke, R.; Novoselov, K. S.; Casiraghi, C. *Nano Lett.* **2012**, *12* (8), 3925–3930.

(41) Zhang, C.; Fu, L.; Liu, N.; Liu, M.; Wang, Y.; Liu, Z. *Adv. Mater.* **2011**, *23* (8), 1020–1024.

(42) Rabti, A.; Raouafi, N.; Merkoçi, A. *Carbon* **2016**, *108*, 481–514.

(43) Takahashi, S.; Anzai, J., *Materials* **2013**, *6* (12), 5742–5762.